MATERIALS SCIENCE & ENGINEERING B

LiMn$_{2-y}$Co$_y$O$_4$ ($0 \leq y \leq 1$) intercalation compounds synthesized from wet-chemical route

N. Amdouni [a,b], F. Gendron [a], A. Mauger [c], H. Zarrouk [b], C.M. Julien [a,*]

[a] *Institut des Nano-Sciences de Paris, CNRS-UMR 7588, Université Pierre et Marie Curie, Campus Boucicaut, 140 Rue de Lourmel, 75015 Paris, France*
[b] *UR Physico-Chimie des Matériaux, Faculté des Sciences de Tunis, Campus Universitaire, 1060 Tunis, Tunisia*
[c] *Département MIPPU, CNRS, campus Boucicaut, 140 rue de Lourmel, 75015 Paris, France*

Abstract

We present the synthesis, characterization and electrode behaviour of LiMn$_{2-y}$Co$_y$O$_4$ ($0 \leq y \leq 1$) spinel oxides prepared by the wet-chemical route assisted by carboxylic acid. The phase evolution was studied as a function of the cobalt substitution and the modification on the intercalation and deintercalation of Li ions. Characterization methods include TG-DTA, XRD, SEM, Raman, FTIR, and SQUID. LiMn$_{2-y}$Co$_y$O$_4$ samples crystallize with the cubic spinel-like structure (*Fd3m* S.G.). Raman scattering and FT-infrared spectroscopy indicate that the vibrational mode frequencies and relative intensities of the bands are sensitive to the covalency of the (Co, Mn)–O bonds. MEB micrographs show that the particle dimension of the LiMn$_{2-y}$Co$_y$O$_4$ powders ranges in the sub-micron-sized domain with a narrow grain-size distribution. The overall electrochemical capacity of LiMn$_{2-y}$Co$_y$O$_4$ oxides have been reduced due to the 3d^6 metal substitution. However, a more stable charge–discharge cycling performances has been observed when the electrodes are charged up to 4.3 V as compared to the performance of the native oxide. For such a cut-off voltage, the charge capacity of the Li//LiMn$_{1.8}$Co$_{0.2}$O$_4$ cell is ca. 101 mA h/g. Differences and similarities between LiMn$_2$O$_4$ and Co-substituted oxides are discussed there from.
© 2006 Elsevier B.V. All rights reserved.

Keywords: Lithium batteries; Co substituted spinels; Lithium insertion; Local structure

1. Introduction

Lithium-ion batteries using transition-metal oxides as positive electrodes are currently dominating the portable power sources industry for laptop computers and mobile telephones. The great success of Li-ion type cells has stimulated studies on high-performance for alternative positive electrodes such as LiMn$_2$O$_4$, but the electrochemical properties of spinel LiMn$_2$O$_4$ are highly dependent on the synthesis route, composition, and thermal history of the samples [1]. Its LiMn$_{2-y}$M$_y$O$_4$ (M = Ni, Co, Al, Cr, Fe, etc.) derivatives exhibiting a high-operating voltage of ca. 4 V are grown by numerous synthesis methods with substitution on the transition-metal site [2,3]. However, LiMn$_2$O$_4$ powders synthesized by the conventional solid-state reaction method shows that the capacity of the 4 V region decreases with increasing annealing temperature above 800 °C [4]. This was attributed to either the larger particle size or to

the deviation from stoichiometry at high synthesis temperatures. In recent years, several wet-chemical techniques including low-temperature preparation such as co-precipitation, sol–gel, and Pechini processes have been successfully developed [5–7]. There are several advantages in using a wet-chemical method to synthesize LiMn$_2$O$_4$ powders: (1) all experiment procedures can be carried out in air, (2) the use of aqueous solution results in an intimate mixture of cations at the molecular level, (3) the synthesis makes an easy control in the ratio of lithium to manganese at low temperatures, and (4) the use of organic-acid gel is particularly attractive for high specific area of obtained powders.

The partial substitution of metal cations for the Mn forming the LiMn$_{2-y}$M$_y$O$_4$ solid solutions (with M = monovalent or multivalent cation) is a strategy to improve significantly the electrochemical cycling of LiMn$_2$O$_4$ materials, but at the expense of a decrease in initial capacity within the useful voltage window, i.e. below 4.4 V. Such a successful result is due to the replacement of the Mn^{3+} Jahn-Teller (JT) ions, which provoke a tetragonal phase transition in the 3 V region [8,9]. Several other origins have been discussed for the reduction of capacity loss
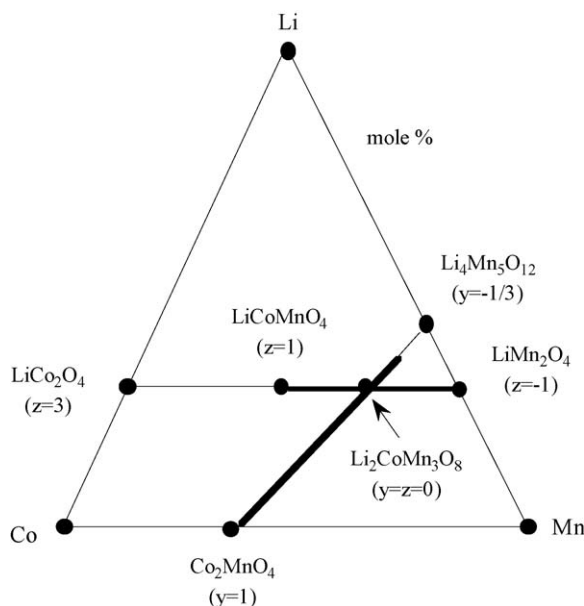
Fig. 1. Formation of spinel solid solutions $Li_2Co_{1+z}Mn_{3-z}O_8$ and $Li_{2-2y}Co_{1+3y}Mn_{3-y}O_8$ (thick lines) in the system Li–Co–Mn–O. Oxygen contents are not specified (from Ref. [10]).

upon cation substitution: (1) the higher M–O bonding strength in the MO_6 framework, (2) stabilization of the spinel lattice by the smaller volume change, (3) the elimination of the two-phase reaction in the upper potential region, (4) the inhibition of the occurrence of the JT distortion, and (5) the decrease of the passivation process occurring on the surface of the electrode. Despite the decreasing first discharge capacity upon substitution, cobalt-doped spinels seem to be the most promising substituted materials investigated so far [9–21].

Several works on the structure and electrochemistry of $LiMn_{2-y}M_yO_4$ oxides prepared by wet-chemistry have been previously reported for cobalt substitution [11–16]. Kawai et al. demonstrated the existence of the $LiMn_2O_4$–$LiCo_2O_4$ solid solution of general formula $Li_2Co_{1+z}Mn_{3-z}O_8$ in the range $-1 \leq z \leq +1$ [10,11]. Two main effects appear with the presence of Co in $LiMn_2O_4$: (1) an enhancement of the exchange current density and (2) an easy charge-transfer reaction of the active material [9]. Single-phase oxides were prepared by lactate [11] and oxalate [13] precursor method, while the $LiCo_{1/6}Mn_{11/6}O_4$ was formed using high-temperature solid-state reaction [14]. Workers have shown that cyclic voltammograms and charge–discharge profiles of the Co-substituted compounds have indicated a structural stabilization associated with an improvement of capacity retention. Fig. 1 shows the phase diagram of the spinel solid solutions $Li_2Co_{1+z}Mn_{3-z}O_8$ and $Li_{2-2y}Co_{1+3y}Mn_{3-y}O_8$ (thick lines) in the system Li–Co–Mn–O. Oxygen contents are not specified [10].

In this contribution, we present the characterization and electrode behaviour of $LiMn_{2-y}Co_yO_4$ ($0 \leq y \leq 1$) prepared by wet-chemistry via the citrate and amino-acetate precursor routes. We study the phase evolution as a function of the cobalt substitution and the modification on the intercalation and deintercala-

tion of Li ions. Characterization methods include X-ray powder diffraction (XRD), thermogravimetry analysis (TG-DTA), scanning electron microscopy (SEM), Raman scattering (RS), Fourier transform infrared (FTIR) spectroscopy, and SQUID magnetometry. The electrochemical charge–discharge profiles of $Li//LiMn_{2-y}Co_yO_4$ ($y = 0.2$) cells are investigated when electrodes are cycled in the potential range of 2.5–4.3 V. Differences and similarities between $LiMn_2O_4$ and Co-substituted oxides are discussed there from.

2. Experimental

Undoped $LiMn_2O_4$ and $LiMn_{2-y}Co_yO_4$ ($0 \leq y \leq 1$) powders were prepared with the same technique, i.e. the carboxylic acid-assisted wet-chemistry, from metal acetates via inorganic polymerization reactions in solution according to the method reported by Julien et al. [22,23]. In this work, both citric and succinic acid were used to compare the final products. These dicarboxylic acids play the role of chelating agent during the synthesis. Stoichiometric amounts of acetate hydrates of Li, Mn, and Co (Fluka, purum p.a. grade) were dissolved in triple distilled water and mixed well with an aqueous solution of either citric or succinic acid (Fluka, MicroSelect grade).

TG-DTA curves of the gel precursors were obtained using a thermogravimetric analyzer (model Netzsch STA 409) at the heating rate of $0.1\,°C\,s^{-1}$ under oxygen flow. The powder XRD patterns have been obtained on a Philips X'Pert PRO MRD (PW3050) diffractometer equipped with a Cu anticathode (Cu Kα radiation λ = 1.54056 Å) at room temperature. The measurements have been recorded under Bragg-Brentano geometry at 2θ with step $0.05°$ in the range of 10–80°. The XRD data were analysed by the Rietveld profile refinements using the Fullprof program. The particle morphology of the $Li(Mn, Co)_2O_4$ powders was examined with a scanning electron microscope (SEM, Philips XL30).

The FTIR absorption spectra were recorded with a Fourier transform interferometer (model Bruker IFS113v) in the wavenumber range of 120–1200 cm^{-1} at a spectral resolution of 2 cm^{-1}. Samples were ground to fine powders and dispersed into ICs pellet. RS spectra were collected with a Raman-laser spectrometer (Jobin-Yvon model U1000) equipped of holographic grating double-monochromator coupled with a spatial filter. Powders were pellized to form mirror-like surface illuminated with the 514.5 nm emission from an Ar-ion laser (model Spectra-Physics 2020). Each RS spectrum was the average of 10 scans collected at a spectral resolution of 1 cm^{-1}. Magnetic measurements were performed in a Quantum Design MPMS SQUID magnetometer. Zero-field-cooled (ZFC) and field-cooled (FC) magnetic susceptibility data were obtained in a field at 1 T in the temperature range of $4 \leq T \leq 300\,K$.

Electrochemical measurements were carried out at room temperature following the experimental procedure previously described using Teflon laboratory-cell hardware and Mac-Pile system [22]. Quasi open-circuit voltage curves were recorded using current pulse of 0.14 mA/cm² applied for 1 h followed by a relaxation period of 0.5–1.0 h, which allows to record the

transient voltage for the determination of chemical diffusion coefficients of Li^+ ions in the $LiMn_{2-y}Co_yO_4$ lattice.

3. Results and discussion

3.1. Synthesis and thermal analysis

Single-phase $LiMn_{2-y}Co_yO_4$ powders were synthesized after further heating of the fluffy brownish black precursors to 400–700 °C in air for 48 h. Both citric and succinic acid acted as fuels due to the presence of carboxylic COOH groups in these complexion agents. They provided decomposition of the metal complexes at low temperature, and yielded the impurity-free $LiMn_{2-y}Co_yO_4$ powders when heated above 400 °C.

Fig. 2a and b shows the TG-DTA curves of $LiMn_{1.6}Co_{0.4}O_4$ gels obtained by both methods. We observe three steps during the course of aqueous solution heat-treatment of citrates and succinates. The weak endothermic effect associated with a weight loss of about 10% for $T < 250$ °C are attributed to departure of residual water. After the departure of the remaining water molecule at 300 °C, a strong exothermic peak appears at ca. 300 °C for citrate (350 °C for succinate) that corresponds to the decomposition of citric acid and acetate ions xerogel. A weight loss of 65.4% occurs during this stage because of the oxidation–decomposition reaction. It appeared that citric acid acts as a fuel in the pyrolysis of the gel precursor, favouring

the decomposition of acetate ions. It was reported that chelating agent (carboxylic-based acid) provokes decomposition during the synthesis of oxide powders [22,23]. The gel precursor was burning because the decomposed acetate ions acted as an oxidizer. Three steps in weight loss at 200–350 °C observed for the succinate route are associated to a more complex decomposition of the remaining organic constituents. Even though the crystallization starts around 400 °C; thus well-crystallized and single $LiMn_{2-y}Co_yO_4$ phases have been obtained at 600 °C. XRD studies after the last effect indicate that very intimately mixed lithium–cobalt–manganese oxides reacted together. Thus, the impurity-free $LiMn_{2-y}Co_yO_4$ oxide has been formed with a spinel structure described in the following. The thermogravimetric results also showed that the exothermic temperature, T_{exo}, attributed to the decomposition–oxidation reaction of the precursor mass increases with addition of cobalt content in $LiMn_{2-y}Co_yO_4$ powders.

3.2. Structure and morphology

The XRD patterns of $LiMn_{2-y}Co_yO_4$ ($0 \leq y \leq 1$) oxides synthesized by sol–gel method from citrate precursors are shown in Fig. 3. Similar results have been obtained using the precipitation method from succinate precursors (see Fig. 4). These data show that all of the compounds are single phase when obtained through a careful selection of precursors. As the substitution of Co^{3+} for Mn^{3+} ions occurs in the $LiMn_2O_4$ spinel structure, a solid solution of lithium cobaltate and lithium manganate is obtained for the $LiMn_{2-y}Co_yO_2$ materials up to $y = 1$. Fig. 4 shows the portions of XRD patterns (in the 2θ range from 50 to 75°) from $LiMn_{2-y}Co_yO_4$ for $0 \leq y \leq 1$ illustrating the lattice parameter shift in the solid solution. As the cobalt content increases a broadening of the diffraction peaks is observed. The XRD patterns of the samples synthesized
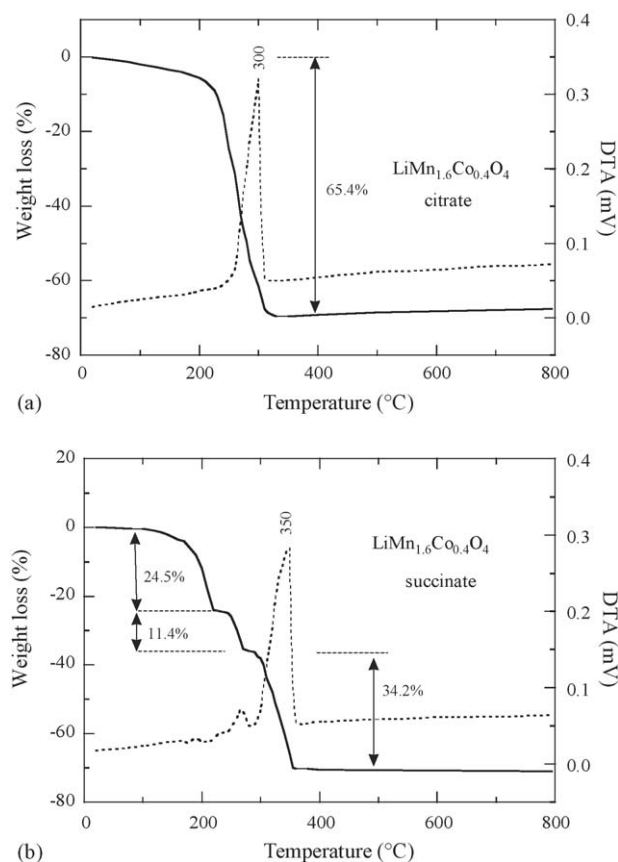

Fig. 2. Thermal analysis of $LiMn_{1.6}Co_{0.4}O_4$ samples synthesized by sol–gel method (a) from citrate route and (b) from succinate route.
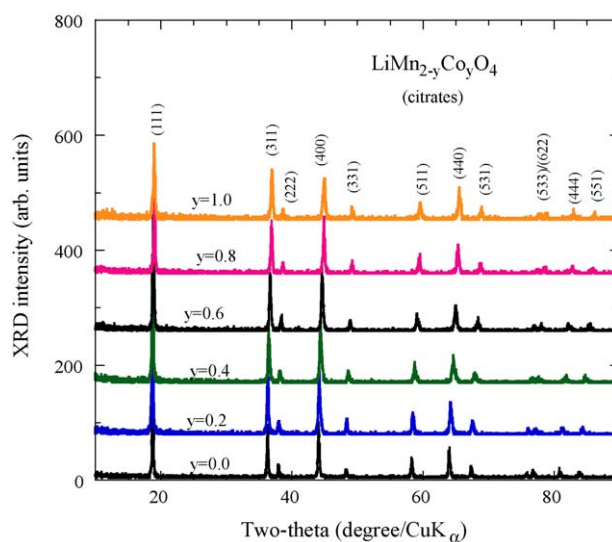

Fig. 3. X-ray diffraction patterns from $LiMn_{2-y}Co_yO_4$ for $0 \leq y \leq 1$ powders synthesized by the sol–gel method from citrate precursors. Powders were fired at 700 °C in air for 48 h. Miller indices of the Bragg peaks are those of the cubic $Fd3m$ space group.
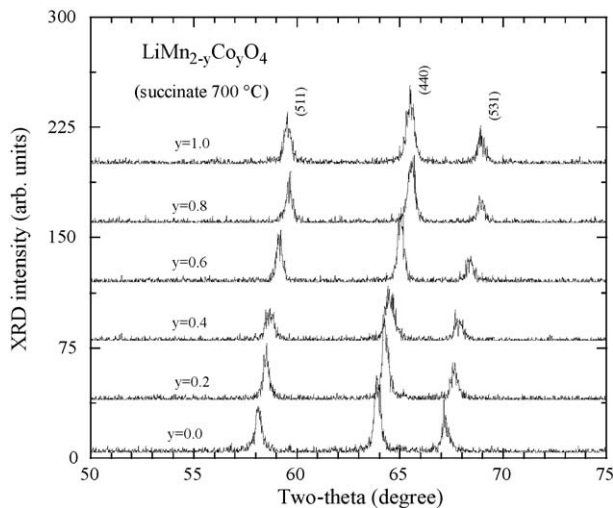
Fig. 4. X-ray diffraction patterns from $LiMn_{2-y}Co_yO_4$ for $0 \le y \le 1$ powders synthesized by the precipitation method from succinate precursors. Limited range (in the 2θ range from 50 to 75°) is shown illustrating the interplanar shifts as the Co content increases the spinel framework.
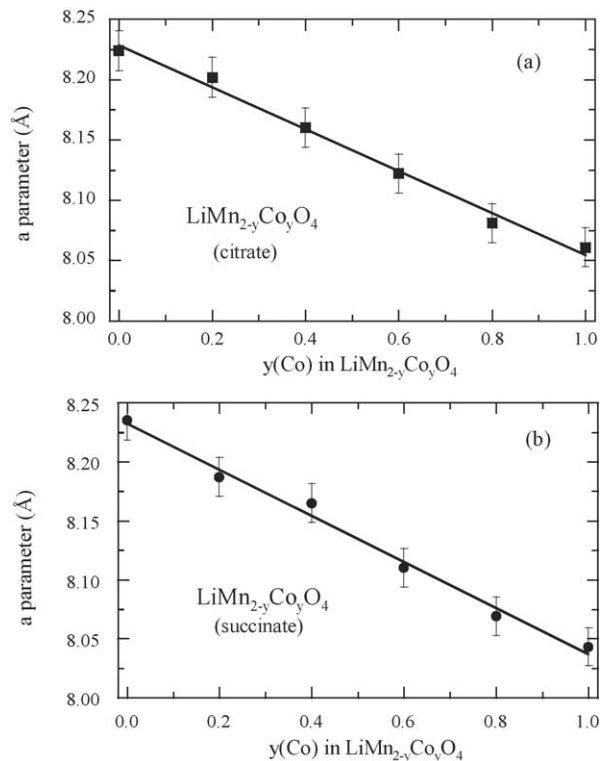

Fig. 5. The lattice parameter of the cubic structure, $Fd3m$ space group, as a function of Co substitution for $LiMn_{2-y}Co_yO_4$ ($0 \le y \le 1$) powders synthesized from (a) citrate and (b) succinate precursors.

for this study were indexed in the cubic $Fd3m$ space group. As compared with that of $LiMn_2O_4$, the lattice parameters of $LiMn_{2-y}Co_yO_4$ decreased with increasing Co content. The (4 4 0) Bragg line and those in the interval $56 \le 2\theta \le 72°$ display a slight displacement due to the decrease of the lattice parameter.

Previous studies have determined the crystal chemistry of $LiMn_{2-y}Co_yO_4$ oxides. They crystallize in the normal spinel structure of general formula $A[B]O_4$. In the spinel structure, lithium (A) ions are located at the tetrahedral 8a sites (Wyckoff notation) and manganese (B) ions are distributed at octahedral 16d sites, while oxygen anions are located at the 32e sites with the oxygen positional parameter, $u = 0.265$. Thus, the 3-D structure of $LiMn_{2-y}Co_yO_4$ is formed by $(Mn, Co)O_6$ octahedra and LiO_4 octahedra. Using electron energy loss spectroscopy [24], XANES [11], EPR [25], magnetic susceptibility measurements [26], and Mn, Co-L-edge XAS and XES spectroscopy [27], it was found that the charge distribution corresponds to $Li[Co_y^{3+}Mn^{4+}Mn_{1-y}^{3+}]O_4$ where Co^{3+} substitutes for Mn^{3+} in the normal $LiMn_2O_4$ spinel. Replacing Mn^{3+} with Co^{3+} (the former is a Jahn-Teller ion while the later is not) minimizes the electrostatic repulsion between the cations occupying 16d octahedral sites of the spinel framework. Despite the great difference in size between Mn^{3+} (ionic radius 0.78 Å for a coordination number of 6) and Co^{3+} (0.68 Å) the favourable stabilizing effect of Co-substitution on the spinel structure accounts for electrochemical improvement upon extended cycles. However, our XRD structure profile refinements suggest that Co replaces Mn^{3+} in the 16d octahedral site, since we do not observe the appearance of a strong (2 2 0) Bragg line (at ca. $2\theta = 30°$), which is extremely sensitive to the occupancy of the 8a tetrahedral site of the spinel lattice.

Fig. 5a and b shows the composition dependence of the lattice parameters of $LiMn_{2-y}Co_yO_4$ ($0 \le y \le 1$) powders synthesized by the sol–gel method from citrate and succinate pre-

cursors, respectively. The cubic parameters calculated via a least-squares refinement method using 14 well-defined XRD lines are $a = 8.061$ (2) and $a = 8.043$ (0) Å for $y(Co) = 1$, respectively. For these materials the spinel structure is well preserved upon considerable cobalt substitution ($y = 1$). As shown in Fig. 5, the replacement of Mn by Co results in a decrease of the cubic parameter; the a-axis shrinks due to the smaller ionic radius of Co^{III} (74 pm) cations, concordant with Co^{3+} substitution for Mn^{3+} and consistent with the results of previous workers [10–23]. It is interesting to remark that the lattice parameter variations are very similar for the different dopants. For $LiMn_{2-y}Co_yO_4$ powders, a microscopic strain in the unit cell due to mismatch of Co^{3+} for Mn^{3+} ions induces the broadening of Bragg peaks (Fig. 4). Note that the cubic parameter for $LiMnCoO_4$ synthesized via succinate is slightly smaller than for citrate route. The variation in the cubic parameter follows an almost Vegard's law.

In general, several factors can contribute to the broadening of peaks in X-ray diffraction [28,29]. For example, the instrumental factors related to the resolution and the incident X-ray wavelength as well as the sample factors such as crystallite size and non-uniform microstrain can cause a line broadening. In the case of an instrumental broadening, the line width will vary smoothly with 2θ or d spacing. On the other hand, the line broadening originating from the sample characteristics will have a different relationship. By combining the Scherrer's equation for crystallite size and the Bragg's law for diffraction, crystallite size and microstrain components are estimated by using the fol-

lowing equation:

$$B^2 \cos^2 \theta = 16\langle e^2 \rangle \sin^2 \theta + \frac{K^2 \lambda^2}{L^2}, \qquad (1)$$

where B is the full-width at half-maximum (fwhm) after correction of the instrumental broadening for finely powdered silicon powder, θ is the diffraction angle, $\langle e^2 \rangle$ denotes local strains (defined as $\Delta d/d$ being the interplanar spacing), L is the crystallite size, and K is a near-unity constant related to crystallite shape.

In Fig. 6 plots for three different reflections for the $LiMn_{2-y}Co_yO_4$ ($y = 0.2$, 0.6, and 1.0) are presented. The slope, $16\langle e^2 \rangle$, and intercept $K^2\lambda^2/L^2$, were used to estimate the distortion and size parameters. Apparently, the integral breadth of Bragg lines of the $y = 1.0$ spinel is slightly greater than those of $y = 0.2$ and 0.6 samples, which suggests a smaller grain size and a higher microstrain content (see Table 1).

Surface morphology and texture as well as particle sizes were observed by scanning electron microscopy (SEM). Fig. 7 shows the typical SEM pictures from $LiMn_{2-y}Co_yO_4$ powders synthesized by the wet-chemical method from citrate precursors. The powders observed by SEM were found to be submicronsized particles, i.e. the grain size average is about 200 nm for $LiMnCoO_4$. The crystallite sizes tended to increase as the sintering time increased, and ranged in size from 100 to 500 nm, suggesting the formation of submicrometre-sized particles with a narrow grain size distribution. The mild conditions used in the
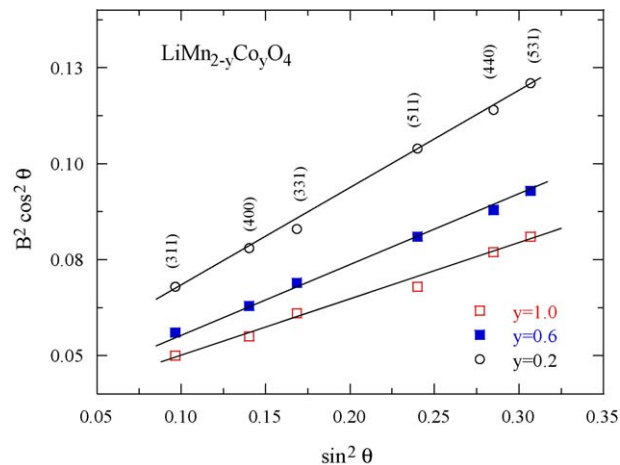

Fig. 6. Plot of $B^2 \cos^2 \theta$ vs. $\sin^2 \theta$ for Bragg lines (3 1 1), (4 0 0), (3 3 1), (5 1 1), (4 4 0), and (5 3 1) of $LiMn_{2-y}Co_yO_4$ ($y = 0.2$, 0.6, and 1.0) samples.

synthesis of the $LiMn_{2-y}Co_yO_4$ spinels explain the small crystallite size that ranges from 200 to 380 nm. These observations are in accordance with the determination made from XRD data (Table 1).

3.3. Vibrational properties

The $LiMn_{2-y}Co_yO_4$ powders annealed at 550 °C were also characterized by means of vibrational spectroscopy to determine
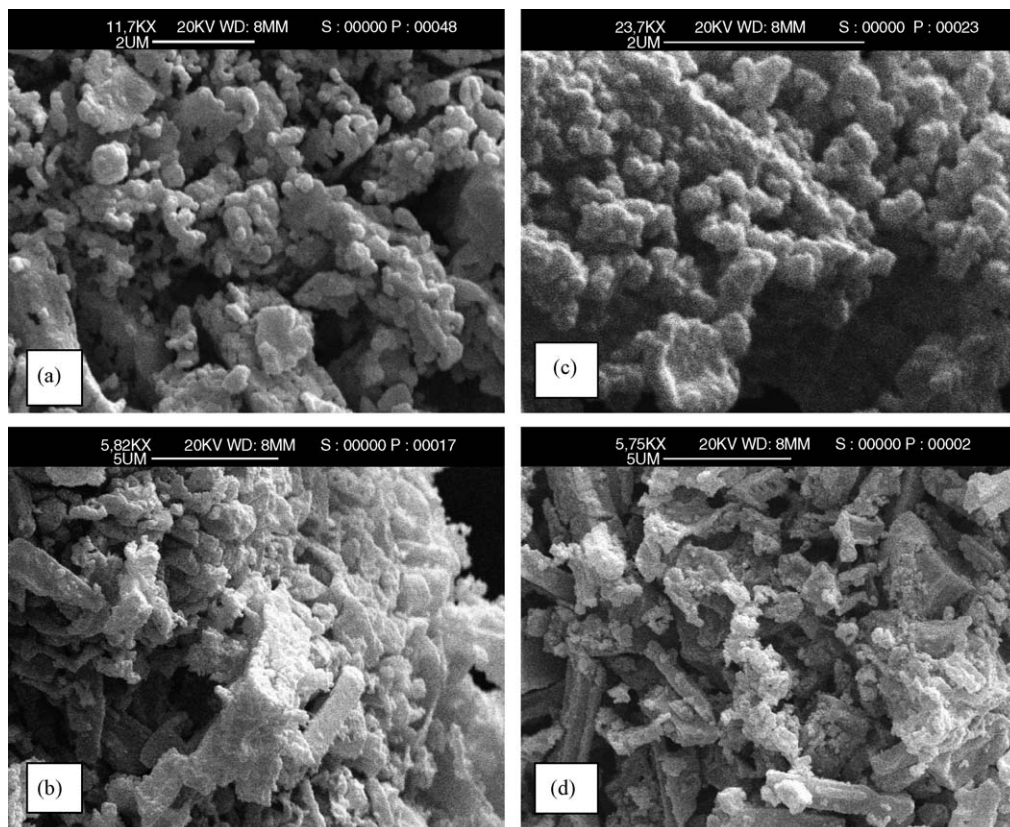

Fig. 7. Scanning electron micrographs of $LiMn_{2-y}Co_yO_4$ powders synthesized by the wet-chemical citrate route for (a) $y = 0.0$, (b) $y = 0.4$, (c) $y = 0.6$, and (d) $y = 1.0$. Submicron-sized particles are observed in these images. White bar on the top is 2 μm.

Table 1
Composition, nominal Mn oxidation state, and structural cubic parameter average of $LiMn_{2-y}Co_yO_4$ ($0.0 \leq y \leq 1.0$) oxides prepared by wet-chemical method from the citrate precursor route

$y(Co)$	Z_{Mn}	a (Å)	L (nm)	$\langle e^2 \rangle \times 10^6$
0.0	3.50	8.224 (0)	229	1.53
0.2	3.55	8.201 (8)	205	1.54
0.4	3.62	8.160 (6)	180	1.59
0.6	3.71	8.122 (0)	170	1.67
0.8	3.83	8.081 (1)	166	1.75
1.0	4.00	8.061 (2)	155	1.83

the local structure and the nature of the cationic environment in the spinel phase. Fig. 8 shows the room temperature RS spectrum of undoped $LiMn_2O_4$ and those of the synthesized $LiMn_{2-y}Co_yO_4$ samples annealed at 700 °C for 48 h with $y = 0.1$ and 0.3. As reported before, the RS spectrum of $LiMn_2O_4$ is dominated by a strong and broad band at ca. 625 cm^{-1} with a shoulder at 580 cm^{-1}. A band with a medium intensity appears at ca. 483 cm^{-1}, while three weak bands are observed at ca. 426, 382, and 300 cm^{-1} [30–32]. RS spectra of $LiMn_{2-y}Co_yO_4$ powders are similar to their $LiMn_2O_4$ counterpart with some additional features.

The cubic spinel possesses the O_h^7 spectroscopic symmetry. Analysis of the vibrational spectra of $LiMn_2O_4$ yields nine optic modes [33]. Five modes are Raman active ($A_{1g} + E_g + 3F_{2g}$) and four are infrared active (F_{1u}). It is also convenient to analyze these spectra in terms of localized vibrations, considering the spinel structure built of MnO_6 octahedra and LiO_4 tetrahedra. For $LiMn_{1.2}Co_{0.8}O_4$, the Raman band located at ca. 639 cm^{-1} can be viewed as the symmetric Mn–O stretching vibration of MnO_6 groups. This band is assigned to the A_{1g} symmetry in the O_h^7 spectroscopic space group. Its broadening is related with
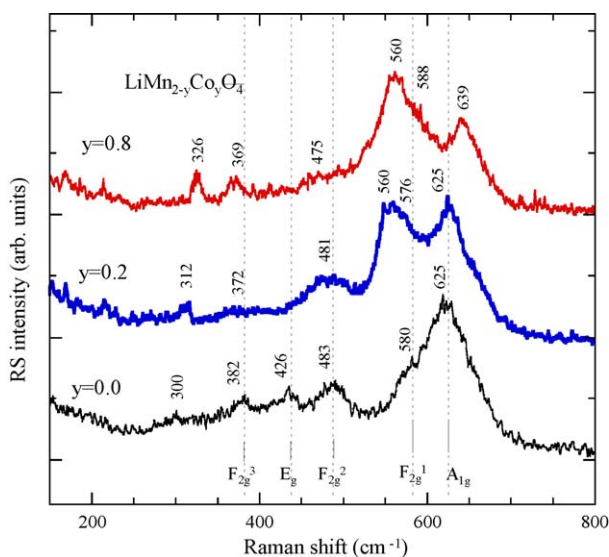
the cation–anion bond lengths and polyhedral distortion occurring in $LiMn_{2-y}Co_yO_4$. The intensity of the shoulder located at 580 cm^{-1} is strongly enhanced upon cobalt substitution. Two components are observed at 588 and 560 cm^{-1}. This may be due to the change of Mn^{3+} and Mn^{4+} proportion versus Co in the material. The RS peaks located at 369 and 475 cm^{-1} have the F_{2g} symmetry. One can state that in the ideal cubic spinel $LiMn_2O_4$, the Mn^{3+} and Mn^{4+} cations are considered as crystallographically equivalent (16d sites) in agreement with XRD data. Then, occupation probabilities of 0.5 must be affected for each cation in 16d site. Hence, a loss of translation invariance certainly occurs in $LiMn_{2-y}Co_yO_4$, due to local lattice distortion around the different Mn^{3+} and Mn^{4+} cations. As a result, a breakdown in the Raman selection rules is expected, which explains the observation of broad bands (disordering in the Mn/Co sublattice) and the fact that more modes than expected are observed in cubic $LiMn_{1.2}Co_{0.8}O_4$.

Fig. 9 shows the FTIR spectra of $LiMn_{2-y}Co_yO_4$ spinel materials at various levels of Co substitution ($0 \leq y \leq 1$). Upon Co substitution, the vibrational modes observed in the far-infrared region appear quite stable. The systematic change in frequency of the high-wavenumber IR bands as a function of Co doping is not surprising, while a blue shift is expected with the increase of Co content due to the shortening of M–O bonds (Fig. 10). The intensity of the stretching mode (F_{1u} symmetry) located at 558 cm^{-1} increases significantly for $y(Co) = 1$, which compares with the shape of the IR feature at 510–570 cm^{-1} for $LiMn_2O_4$. These results show that the local environment of lithium ions surrounded by oxygen anions is not strongly affected and the
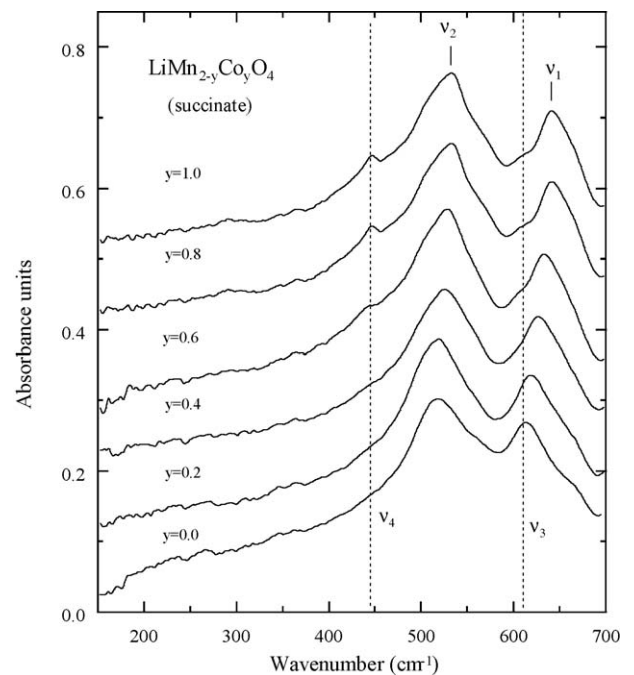

Fig. 8. Raman scattering spectra of $LiMn_{2-y}Co_yO_4$ (for $y = 0.0$, 0.2, and 0.8) oxide powders synthesized by the sol–gel method from citrate precursors fired at 700 °C in air for 48 h. Vertical lines visualize the position of the bands identified as intrinsic modes for the $LiMn_2O_4$ spinel.

Fig. 9. FTIR absorption spectra of $LiMn_{2-y}Co_yO_4$ (for $0.0 \leq y \leq 1.0$) oxide powders synthesized by the sol–gel method from succinate precursors fired at 700 °C in air for 48 h. The vertical lines visualize the position of the ν_3 and ν_4 bands identified as additional modes due to Co–O bonds.
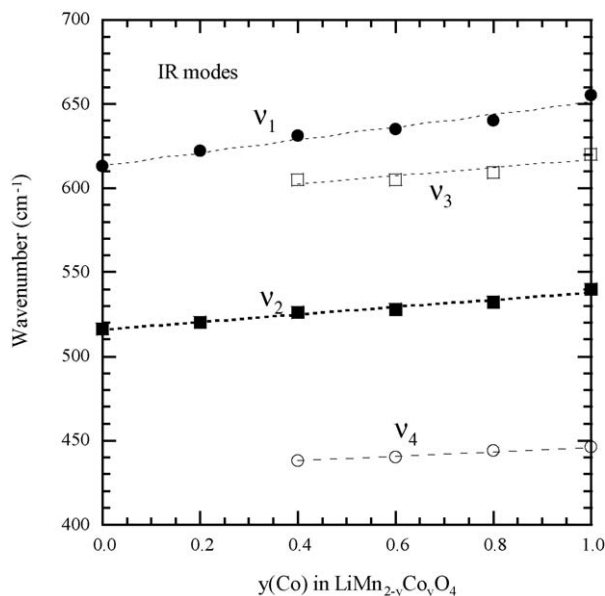
Fig. 10. Composition dependence of the frequency of IR modes observed in Fig. 9. Wavenumbers were determined from a fit using Gaussian shape of the bands.

covalency of MnO_6 units increased slightly with doping. For high level of Co substitution, the broadening of the infrared peaks can be interpreted as an increase in MnO_6 distortion due to the incorporation of Co^{3+} ions in the MO_6 octahedra. However, because the stability of the LiO_4 stretch, we can conclude that Co^{3+} cations were not incorporated on the Li sites of the interlayer space. Two new IR bands noted ν_3 and ν_4 appear with increasing Co content. They are located at ca. 440 and 610 cm^{-1}. These new modes are assigned to the bending and stretching of Co–O bonds, respectively.

3.4. Electronic properties

Fig. 11 displays the Arrhenius plots of the σT of $LiMn_{2-y}Co_yO_4$ compounds where σ is the electrical conduc-
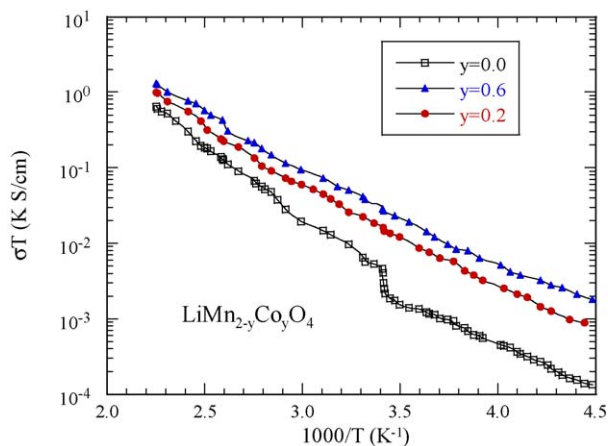

Fig. 11. Plot of σT vs. reciprocal temperature for $LiMn_2O_4$ and Co-substituted $LiMn_{2-y}Co_yO_4$ spinels synthesized from citrate precursors.

tivity. These graphs show that over the compositional range $0.0 \leq y \leq 0.6$ the conductivity is thermally activated owing to the semiconducting character of these oxides. The electrical conductivity varies from 10^{-8} to 10^{-2} S/cm in the temperature range from 220 to 450 K. Examination of the data (Fig. 11) indicates that (i) the electrical conductivity is sensitive to the introduction of $Co^{3+}(3d^6)$ ions in the host lattice, (ii) a noticeable change in the activation energy is observed in the high-temperature region, (iii) the temperature dependence of σ_{dc} deviates markedly from the exponential law—a curvature appears in the Arrhenius plots, and (iv) the phase transition nearby ambient temperature disappears for Co-doped $LiMn_2O_4$. The room temperature electrical conductivity increases by one order of magnitude from 10^{-5} S/cm for $LiMn_2O_4$ to 10^{-4} S/cm for $LiMn_{1.4}Co_{0.6}O_4$.

According to the electronic considerations discussed by Goodenough et al. [34], the small-polaron semiconducting character of the $Li[Mn^{3+}Mn^{4+}]O_4$ compound is due to weak Mn–Mn interactions, which prevents an itinerant-electron bandwidth, hence localized electronic configurations. Considering the model of small-polaron transport suggested by Austin and Mott [35], the d.c. conductivity should be given by:

$$\sigma_h = \frac{AC(1-C)}{T} \exp\left(-2\alpha R - \frac{W}{k_B T}\right), \qquad (2)$$

where A is a constant, C is the concentration of one type of cation, R is the average interionic separation, α^{-1} is the radius of the localized wavefunction (usually ≈ 10 Å in transition metal oxides), W is the activation energy, T is the absolute temperature, and k_B is the Boltzman constant. For the undoped $LiMn_2O_4$ spinel, the room temperature conductivity is ca. 10^{-5} S/cm and the activation energy is 0.161 eV. These values are typical of small-polaron conduction in a mixed-valent system. In fact, the $LiMn_2O_4$ material imposes equal quantity of Mn^{4+} and Mn^{3+} ions per formula unit, which allows for easy transfer of electrons via hopping. The Co substitution increases the average valency of the manganese ions from $Mn^{3.50+}$ for cubic structure $LiMn_2O_4$ to $Mn^{3.71+}$ for the $LiMn_{1.4}Co_{0.6}O_4$ phase. Thus the electrical conductivity of lithium manganese oxides with the spinel structure depends strongly on the cationic valence state and their distribution among the crystallographic positions in the framework. Enhancement of the electrical conductivity originates from three factors: (1) the increase of carrier concentration due to the change in the average valency Z_{Mn} (Table 1), (2) the decrease of the M–O distances in the structure which reduces the average interionic separation, and (3) the decrease of the activation energy due to the slight modification of the electronic band structure upon Co substitution. In addition, we observed the disappearance of the phase transition, which occurs nearby room temperature in undoped $LiMn_2O_4$. This first-order phase transition has been attributed to a cooperative effect of the Jahn-Teller Mn^{3+} ions [36,37]. The distortion is suppressed by cobalt substitution due to an increase of the average Mn valency. A loss of translation invariance certainly occurs, due to local lattice distortions around the different Mn^{3+} and Mn^{4+} cations.
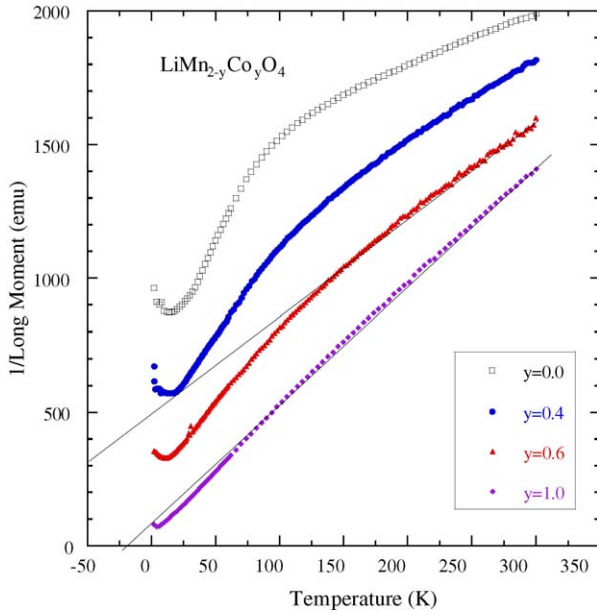
Fig. 12. Reciprocal magnetic susceptibility of Co-substituted spinel LiMn$_{2-y}$Co$_y$O$_4$. Solid lines visualize the linear plot of the Curie–Weiss law of the paramagnetic region.

3.5. Magnetic properties

Fig. 12 shows the temperature dependence of the magnetic susceptibility of LiMn$_{2-y}$Co$_y$O$_4$ ($0 \leq y \leq 1$) samples. In the low-temperature region, a drastic change in magnetization is observed upon substitution of Co for Mn. In particular, the strong anomaly at $T = 30$ K disappears progressively with the introduction of Co^{3+} in the spinel lattice. This is a consequence of the disappearance of the Mn^{3+} ions in the [Mn$_2$]O$_4$ sublattice. For LiCoMnO$_4$, Mn^{4+} are the only paramagnetic species if we assume that low-spin Co^{3+} ions are diamagnetic species as confirmed below. In the entire temperature range (5–300 K), the sample $y = 1.0$ follows a paramagnetic behavior. The curves $\chi_m^{-1}(T)$ can be represented by a straight line obey-

Table 2
Curie constant and Weiss temperature for LiMn$_{2-y}$Co$_y$O$_4$ phases synthesized by citrate route

y(Co)	C_p (emu K/mol)		θ_p (K)
	Theoretical[a]	Experimental	
0.0	4.83	4.79	−262
0.2	4.24	4.25	−230
0.4	3.64	3.62	−195
0.6	3.05	3.10	−140
0.8	2.45	2.50	−85
1.0	1.86	1.92	−20

[a] Calculated Curie constants were obtained by assuming that Co ions are in low-spin +3 state.

ing the Curie–Weiss law that allows to determine the magnetic constants:

$$\chi_m^{-1} = \frac{N_A p_{eff}^2 \mu_B^2}{3k_B} \frac{1}{T - \theta_p} = \frac{C_p}{T - \theta_p}, \tag{3}$$

where N_A is the Avogadro' number, k_B is the Boltzman' constant, μ_{eff} is the Bohr magneton, p_{eff} is the effective magnetic moment number, θ_p is the Weiss temperature in K, and C_p is the Curie constant in emu K/mol. The Curie constant and Weiss temperature for LiMn$_{2-y}$Co$_y$O$_4$ compounds are reported in Table 2. The effective magnetic moment number of LiMn$_{2-y}$Co$_y$O$_4$ spinels is obtained from the sum of the magnetic susceptibility of each magnetic ion, as follows:

$$p_{eff}^2 = p_{Mn^{4+}}^2 + (1 - y)p_{Mn^{3+}}^2 + y p_{Co^{3+}}^2, \tag{4}$$

where, $p_{Mn^{4+}}$, $p_{Mn^{3+}}$, and $p_{Co^{3+}}$ are the spin-only paramagnetic moment numbers of Mn^{4+}, Mn^{3+}, and Co^{3+}, respectively. Spin-only numbers are calculated in the case of quenched angular momentum using $p = 2[S(S+1)]^{1/2}$ where S is the spin quantum number. The theoretical values of the Curie constant (Table 2) were calculated using the spin-only values of $\mu_{eff} = 3.87\mu_B$ ($S = 3/2$) and $4.90\mu_B$ ($S = 2$) for magnetic moments of Mn^{4+} and Mn^{3+}, respectively [38].
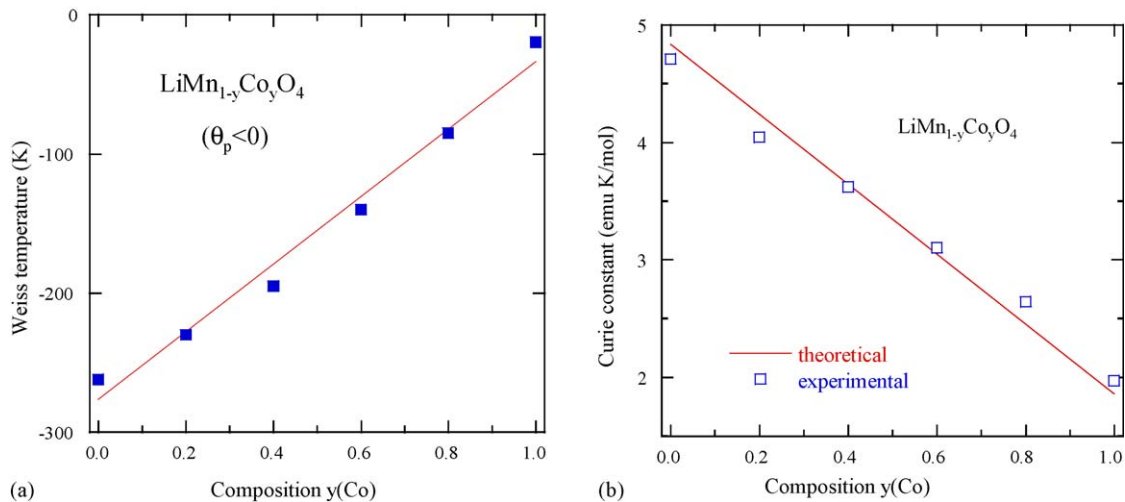

Fig. 13. Composition dependence of (a) the Weiss temperature θ_p and (b) the Curie constant C_p for LiMn$_{2-y}$Co$_y$O$_4$ spinel. Data were obtained from the linear fits of the paramagnetic behavior fin Fig. 12. Solid line in (b) represents the theoretical curve using Eq. (5).
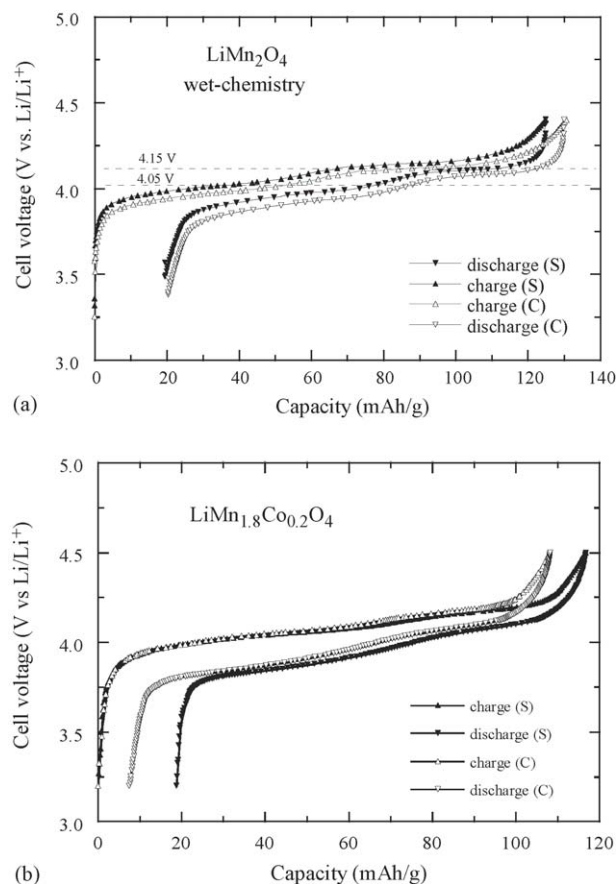
Fig. 14. Charge–discharge profiles of (a) Li//LiMn$_2$O$_4$ and (b) Li//LiMn$_{1.8}$Co$_{0.2}$O$_4$ cells using electrodes grown by wet-chemistry using citrate (C) and succinate (S) precursor. The quasi-open voltage curves were obtained by GITT method with current density 0.14 mA/cm^2 (C/20 rate).

The very large negative Weiss temperature $\theta_p = -260$ K for LiMnO$_4$ decreases to $\theta_p = -20$ K for LiMnCoO$_4$ indicating a weaker antiferromagnetic interactions. Hence, it appears that Mn^{4+} in a [Mn^{4+}Co^{3+}] environment is a stable configuration at low temperature. This observation suggests that the cobalt ions themselves must impart a larger electron spin density through the metal–oxygen–lithium bond in addition to the increasing presence of Mn^{4+}. Fig. 13 shows the composition dependence of the Weiss temperature, θ_p, and the Curie constant, C_p, for LiMn$_{2-y}$Co$_y$O$_4$ spinel. Data were obtained from the linear fits of the paramagnetic behavior in Fig. 12. Solid line in Fig. 12 represents the theoretical curve using Eqs. (4) and (5) using a low-spin Co^{3+} ($S = 0$). We observe a good agreement between theoretical and experimental values showing that, as expected, the Co^{3+} ions are in the low-spin configuration.

3.6. Electrochemical properties

The electrochemical features of synthesized spinel LiMn$_{2-y}$Co$_y$O$_4$ were examined using Li//LiMn$_{2-y}$Co$_y$O$_4$ cells submitted to constant current cycling, i.e. under galvanostatic conditions at 22 °C. The results from the electrochemical Li//LiMn$_2$O$_4$ cell are presented in Fig. 14a. The cells were charged and discharged at current densities of 0.14 mA/cm^2 or 16 mA/g, while the volt-

Table 3
Electrochemical properties of LiMn$_{2-y}$Co$_y$O$_4$ phases synthesized by wet-chemistry from citrate (c) and succinate (s) precursors

Material	Theoretical capacity (mA h/g)	Δx	Practical capacity[a] (mA h/g)	Efficiency (%)
LiMn$_2$O$_4$	125	0.85	110	83
LiMn$_{1.8}$Co$_{0.2}$O$_4$ (c)	123	0.80	101	82
LiMn$_{1.8}$Co$_{0.2}$O$_4$ (s)	123	0.80	98	80

The theoretical capacity is based on the mass of the fully oxidized composition at 4.3 V.

[a] For the first discharge process.

age is monitored between 3.0 and 4.4 V. In this potential domain, the charge–discharge curves of materials synthesized by wet-chemistry correspond to the voltage profiles characteristic of the LiMn$_2$O$_4$ ceramic material associated with lithium occupancy of tetrahedral sites. From the variation of the cell potential for the complete cell (Fig. 14a), one can see the presence of two regions during the lithium insertion–extraction processes. The shape of the voltage curves indicates whether the delithiated Li$_{1-x}$Mn$_2$O$_4$ exists as a multiple-phase system. The first region (I) is characterized by an S-shaped voltage curve, whereas the second region (II) corresponds to a plateau portion. In region I, the charge voltage increases continuously in the voltage range of 3.80–4.05 V. In region II, the charge voltage is stable around 4.15 V. However, electrode materials prepared from the citrate route provide a higher capacity (101 mA h/g) than oxides synthesized by the co-precipitation technique (97 mA h/g). This slight difference is attributed to the powder morphology (Table 3).

For the Li//LiMn$_{1.8}$Co$_{0.2}$O$_4$ cell (Fig. 14b), the upper 4 V plateau provides over 98 mA h/g based on the active material utilisation with an excellent cyclability. It is obvious that the initial capacity is decreased with increasing the Co content. This is due to the decreasing amount of Mn^{3+} ions in the substituted spinel phase since during the intercalation–deintercalation of Li$^+$ in LiMn$_2$O$_4$ only the amount of Mn^{3+} contributes to the charge capacity. Charge and discharge tests for both citrate and succinate LiMn$_{1.8}$Co$_{0.2}$O$_4$ show the better performance of the former electrode in terms of capacity retention. A unique pseudo one-phase is observed during charge–discharge process when electrodes are cycled in the voltage range of 2.8–4.4 V (Fig. 14b). The electrochemical stability has been attributed to the suppression of the Jahn-Teller distortion caused by Mn^{3+} ions and to the stronger metal–oxygen bonding in substituted LiMn$_{2-y}$Co$_y$O$_4$ spinel phases. In compound like LiMn$_{2-y}$Co$_y$O$_4$, Mn would have an average oxidation number of 3.59, corresponding to a Mn^{3+}:Mn^{4+} ratio of 41:59, which would make ratios smaller than 1 more probable in the final discharge stage. In LiMn$_{1.8}$Co$_{0.2}$O$_4$, the Mn oxidation number is 3.53, which is close to the theoretical value for undoped spinel. This suggests that the electrochemical stability of this compound is less than the former one.

The inverse derivative ($-\partial Q/\partial V$) plots versus cell voltage for LiMn$_{1.8}$Co$_{0.2}$O$_4$ are shown in Fig. 15. This type of graph is very informative because plateaus in voltage versus capacity give rise to peaks in ($-\partial Q/\partial V$); so derivative plots are useful for display-
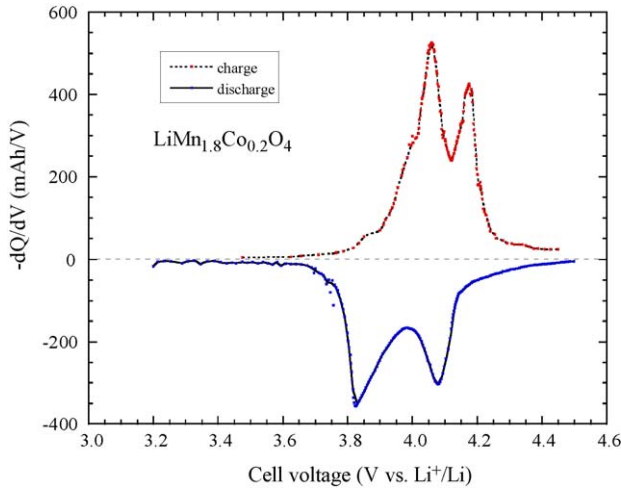
Fig. 15. Plot of the incremental derivative capacity $(-\partial Q/\partial V)$ for the Li//LiMn$_{1.8}$Co$_{0.2}$O$_4$ cell as a function of the cell voltage vs. Li/Li$^+$ for the first charge–discharge process.

Fig. 17. Evolution of the chemical diffusion coefficient D^*_{Li} of Li$^+$ ions as a function of the Li composition in Li$_x$Mn$_{1.8}$Co$_{0.2}$O$_4$. Powders were synthesized by the wet-chemical citrate route. Squares are experimental data measured during the discharge. Fits were made using Eq. (6).

ing details. The two regimes of intercalation in LiMn$_{1.8}$Co$_{0.2}$O$_4$ are clearly depicted when derivative voltage $(-\partial Q/\partial V)$ is plotted versus cell voltage. A broad bands centered at 4.05 V (capacity around $x = 0.7$) is indicative of the one-phase system, while the narrow band at 4.15 V (capacity around 0.4) is indicative of the two-phase system. For the Li//LiMn$_{1.8}$Co$_{0.2}$O$_4$ cell, the upper 4 V plateau provides over 100 mA h/g based on the active material utilisation with an excellent cyclability.

Fig. 16 shows the discharge capacity versus cycle number for Li//LiMn$_{1.8}$Co$_{0.2}$O$_4$ cells (citrate and succinate) compared with the native LiMn$_2$O$_4$ oxide. The Co-substituted products have been found to be excellent in terms of practical material utilisation. Obviously, the Co incorporation improves the cyclability of the Li//LiMn$_{2-y}$Co$_y$O$_4$ cells. The substituted LiMn$_{2-y}$Co$_y$O$_4$ spinel phases are more stable than LiMn$_2$O$_4$. For $y = 0.2$, the capacity fading is less than 5% at the 35th cycle for the electrode material synthesized from citrate precursor. From the comparison between electrodes prepared from different precursors, we can conclude that the better crystallinity, the finer and
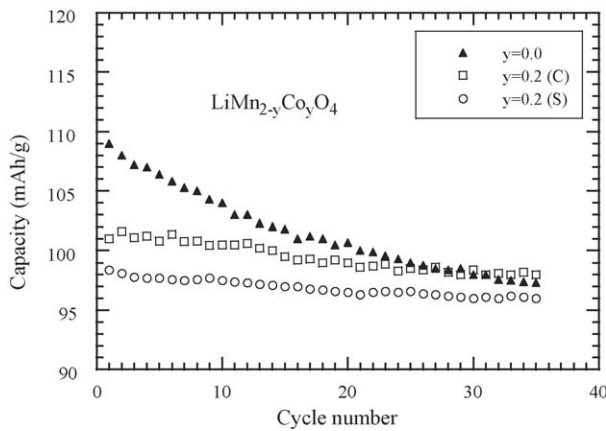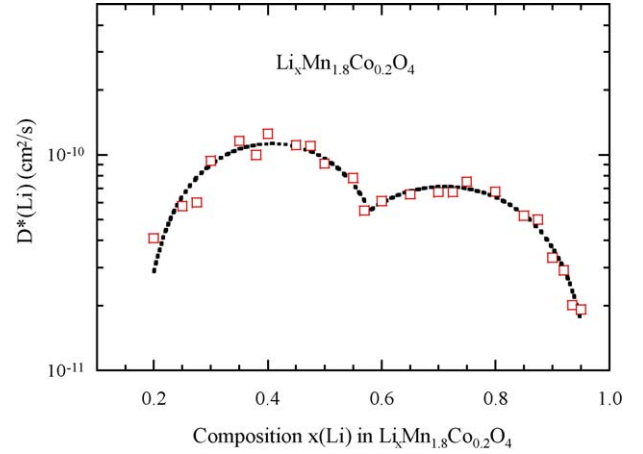

Fig. 16. Discharge capacity vs. cycle number for Li//LiMn$_{1.8}$Co$_{0.2}$O$_4$ cells compared with that of Li//LiMn$_2$O$_4$. Positive electrodes were synthesized by citrate (C) and succinate (S) route.

more homogeneous particles of LiMn$_{1.8}$Co$_{0.2}$O$_4$ by the sol–gel method, compared with those by the coprecipitation method, are considered to lead to larger discharge capacities. The improvement of the cyclability observed for LiMn$_{1.8}$Co$_{0.2}$O$_4$ seems to be related to the stronger M–O bonds in the [M$_2$]O$_4$ sublattice. This can be attributed to the higher ligand field stabilization energy of the Co^{3+}($t_{2g}^6 e_g^0$) compared to the Mn^{3+}($t_{2g}^3 e_g^1$) ions [39].

The determination of the chemical diffusion coefficients of lithium ions in positive electrodes was done by the GITT method. This technique consists of a series of current steps separated by a relaxation period. For short times and small current pulses, the solution of the infinite diffusion problem, based on the early work of Weppner and Huggins [40], leads to a simple expression for the chemical diffusivity, D^*_{Li}, of lithium ions if the pulse duration, t, is smaller than the characteristic time $\tau = L^2/D^*_{Li}$:

$$D^*_{Li} = \frac{4}{\pi t}\left(\frac{m V_m}{MS}\right)^2\left(\frac{\Delta E_s}{\Delta E_t}\right)^2 \qquad (5)$$

where S is the surface area, and ΔE_t and ΔE_s are the voltage changes during the current pulse and after the current pulse, respectively. m, M, and V_m are the mass, molecular weight, and partial molar volume of the host oxide, respectively. The high insertion capability has been confirmed also by measuring the chemical diffusion coefficients of Li$^+$ ions in Li$_x$Mn$_{1-y}$Co$_y$O$_2$ materials. Fig. 17 shows the evolution of the chemical diffusion coefficient D^*_{Li} of Li$^+$ ions in LiMn$_{1.8}$Co$_{0.2}$O$_4$ sample synthesized by the wet-chemical citrate route. D^*_{Li} are in the vicinity of 10^{-10}–10^{-11} cm^2/s during the discharge of the Li//LiMn$_{1.8}$Co$_{0.2}$O$_4$ cell.

If we consider that the diffusion of Li ions into the host matrix has two limiting factors, the ion hopping probability and the degree of site occupancy, then the chemical diffusion coefficient can be expressed as:

$$D^*_{Li} = \alpha W[(x_m - x)^2 + \beta(x_m - x)], \qquad (6)$$

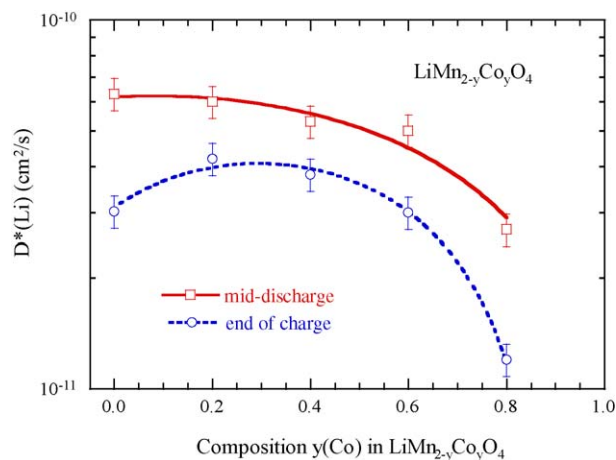where x_m is the full site occupancy for Li ions, α is the factor related with the probability for ion hopping, and β represents

Fig. 18. Evolution of the chemical diffusion coefficient D_{Li}^* of Li$^+$ ions in LiMn$_{2-y}$Co$_y$O$_4$ powders synthesized by the wet-chemical citrate route. Squares and circles are experimental data measured at mid-discharge and end of charge, respectively. Fits were made using Eq. (7).

an interaction factor [41]. Lines in Fig. 17 are the curves calculated from Eq. (6) giving parameters $\alpha = 1.1 \times 10^{-11}$ cm^2/s and $\beta = 5.8$ for LiMn$_{1.8}$Co$_{0.2}$O$_4$. These features reflecting the relatively facile extraction process for Li ions in the LiMn$_{1.8}$Co$_{0.2}$O$_4$ spinel structure synthesized by the wet-chemical technique are in good accordance with SEM and XRD data. It is necessary to obtain sub-micrometer particles of uniform morphology with narrow size distribution and homogeneity in order to achieve the reliability of the lithium batteries.

Fig. 18 shows the evolution of the chemical diffusion coefficient D_{Li}^* of Li$^+$ ions as a function of the Co content in LiMn$_{2-y}$Co$_y$O$_4$ powders synthesized by the wet-chemical citrate route. Squares and circles are experimental data measured at mid-discharge and at the end of charge, respectively. Fits were made using a simple polynomial equation as follows:

$$D_{Li}^* = D_0 + \alpha y + \beta y^2, \tag{7}$$

where D_0 is in the range of 3–5 × 10^{-11} cm^2/s. Data shown in Fig. 18 exhibit an increase up to $y = 0.4$ and then decrease considerably in the range of 6–1 × 10^{-11} cm^2/s. Based on the crystal structure of LiMn$_{2-y}$Co$_y$O$_4$ spinel phases, the intercalation process is partly controlled by the number of Li$^+$ ion occupancies in the host lattice (geometrical factor) but also by the number of redox species (Mn^{3+}/Mn^{4+}). The cobalt substitution also provides an increase of chemical diffusion coefficients of Li ions in the LiMn$_{1.8}$Co$_{0.2}$O$_4$ lattice.

4. Conclusion

In this work, we have studied the structural, physical, and electrochemical properties of Co-substituted LiMn$_{2-y}$Co$_y$O$_4$ ($0 \leq y \leq 1$) positive electrode materials synthesized by a sol–gel method from citrate and succinate precursors. X-ray diffraction patterns, Raman scattering, FTIR, and magnetic measurements have shown that single-phase impurity free can be made through careful selection of precursors. Vibrational spectroscopies have shown that, for moderate Co substitution, the local octahedral

environment of Li ions in LiMn$_{2-y}$Co$_y$O$_4$ is almost similar to that in LiMn$_2$O$_4$.

The voltage profiles of the layered substituted oxides monitored against lithium electrode show that the overall capacity of positive electrodes was reduced due to the 3d^6-metal substitution. However, more stable charge–discharge cycling performances have been observed when electrodes are charged up to 4.3 V as compared to the performances of the native oxides. The rechargeability of the Li//LiMn$_{2-y}$Co$_y$O$_4$ cells appears better than LiMn$_2$O$_4$ because the lack of high concentration of Mn^{3+} ions in the low-voltage region. The improvement of the cyclability observed for LiMn$_{1.8}$Co$_{0.2}$O$_4$ seems to be also related to the stronger M–O bonds in the [M$_2$]O$_4$ sublattice. This can be attributed to the higher ligand field stabilization energy of the Co^{3+}($t_{2g}^6 e_g^0$) compared to the Mn^{3+}($t_{2g}^3 e_g^1$) ions. For the Li//LiMn$_{1.8}$Co$_{0.2}$O$_4$ cell, the upper 4 V plateau provides over 101 mA h/g based on the active material utilisation with an excellent cyclability.

References

[1] M.M. Thackeray, W.I.F. David, P.G. Bruce, J.B. Goodenough, Mater. Res. Bull. 18 (1983) 461.
[2] M.M. Thackeray, Prog. Solid State Chem. 25 (1998) 1.
[3] M. Wakihara, Mater. Sci. Eng. R 38 (2001) 1.
[4] A. Momchilov, V. Manev, A. Nassalevska, J. Power Sources 41 (1993) 305.
[5] P. Barboux, J.M. Tarascon, F.K. Shokoohi, J. Solid State Chem. 94 (1991) 185.
[6] S.R.S. Prabaharan, S.S. Michael, C. Julien, Int. J. Inorg. Mater. 1 (1999) 21.
[7] W. Liu, G.C. Farrington, F. Chaput, B. Duhn, J. Electrochem. Soc. 143 (1996) 879.
[8] Y. Xia, M. Yoshio, J. Electrochem. Soc. 143 (1996) 825.
[9] M. Wakihara, L. Guohua, H. Ikuta, T. Uchida, Solid State Ionics 86–88 (1996) 907.
[10] H. Kawai, M. Nagata, H. Tukamoto, A.R. West, Electrochim. Solid State Lett. 1 (1998) 2123.
[11] H. Kawai, M. Nagata, H. Kageyama, H. Tukamoto, A.R. West, Electrochim. Acta 45 (1999) 315.
[12] A.R. West, H. Kawai, H. Kageyama, M. Tabuchi, M. Nagata, H. Tukamoto, J. Mater. Chem. 11 (2001) 1662.
[13] L. Guohua, H. Ikuta, T. Uchida, M. Wakihara, J. Electrochem. Soc. 143 (1996) 178.
[14] B. Banov, Y. Yodorov, A. Trifonova, A. Momchilov, V. Manev, J. Power Sources 68 (1997) 758.
[15] P. Arora, B.N. Popov, R.E. White, J. Electrochem. Soc. 145 (1998) 807.
[16] D. Song, H. Ikuta, T. Uchida, M. Wakihara, Solid State Ionics 117 (1999) 151.
[17] H.J. Bang, V.S. Donepudi, J. Prakash, Electrochem. Soc. Proc. 2000-21 (2000) 33.
[18] J.M. Amarilla, J.L. Martin de Vdales, R.M. Rojas, Solid State Ionics 127 (2000) 73.

[19] E. Zhecheva, R. Stoyanova, M. Gorova, P. Lavela, J.L. Tirado, Solid State Ionics 140 (2001) 19.

[20] K.M. Shaju, G.V. Subba Rao, B.V.R. Chowdari, Solid State Ionics 148 (2002) 343.

[21] B.W. Lee, J. Power Sources 109 (2002) 220.

[22] C. Julien, L. El-Farh, S. Rangan, M. Massot, J. Sol-Gel Sci. Technol. 15 (1999) 63.

[23] C. Julien, M.S. Michael, S. Ziolkiewicz, Int. J. Inorg. Mater. 1 (1999) 29.

[24] S. Suzuki, M. Tomita, S. Okada, H. Arai, J. Phys. Chem. Solids 57 (1996) 1851.

[25] R. Stoyanova, E. Zhacheva, M. Gorova, J. Mater. Chem. 10 (2000) 1377.

[26] B. Gee, C.R. Horne, E.J. Cairns, J.A. Reimer, J. Phys. Chem. B 102 (1998) 10142.

[27] M.M. Grush, C.R. Horne, R.C.C. Perera, D.L. Ederer, S.P. Cramer, E.J. Cairns, T.A. Callcott, Chem. Mater. 12 (2000) 659.

[28] H.P. Klug, L.E. Alexander, X-Ray Diffraction Procedures for Polycrystalline and Amorphous Materials, Wiley, New York, 1974.

[29] C. Hammond, The Basic of Crystallography and Diffraction, Oxford University Press, New York, 1997.

[30] C. Julien, G.A. Nazri, Mater. Res. Soc. Symp. Proc. 548 (1999) 79.

[31] C. Julien, A. Rougier, E. Haro-Poniatowski, G.A. Nazri, Mol. Cryst. Liq. Cryst. 311 (1998) 81.

[32] C. Julien, in: C. Julien, Z. Stoynov (Eds.), Materials for Lithium-Ion Batteries, NATO-ASI Series, vol. 3–85, Kluwer Acad. Publ., Dortrecht, 2000, p. 309.

[33] G.C. Allen, M. Paul, Appl. Spectrosc. 49 (1995) 451.

[34] J.B. Goodenough, A. Manthiran, A.C.W.P. James, P. Strobel, Mater. Res. Soc. Symp. Proc. 135 (1989) 391.

[35] I.G. Austin, N.F. Mott, Adv. Phys. 18 (1969) 41.

[36] A. Yamada, M. Tanaka, Mater. Res. Bull. 30 (1995) 715.

[37] A. Yamada, J. Solid State Chem. 122 (1996) 160.

[38] C. Kittel, Introduction to Solid State Physics, 2nd ed., John Wiley & Sons, New York, 1956.

[39] L. Hernan, J. Morales, L. Sanchez, J. Santos, Solid State Ionics 118 (1999) 179.

[40] W. Weppner, R.A. Huggins, J. Electrochem. Soc. 124 (1977) 1569.

[41] B. Yebka, C. Julien, Solid State Ionics 90 (1996) 141.